

pubs.acs.org/JPCC Article

# Crystallization of the P<sub>3</sub>Sn<sub>4</sub> Phase upon Cooling P<sub>2</sub>Sn<sub>5</sub> Liquid by Molecular Dynamics Simulation Using a Machine Learning Interatomic Potential

Chao Zhang, Yang Sun, Hai-Di Wang, Feng Zhang, Tong-Qi Wen, Kai-Ming Ho, and Cai-Zhuang Wang\*



Cite This: J. Phys. Chem. C 2021, 125, 3127–3133



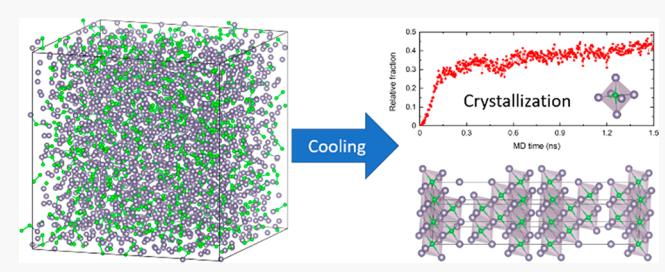
**ACCESS** 

Metrics & More

Article Recommendations

Supporting Information

**ABSTRACT:** We performed molecular dynamics simulations to study the crystallization of the  $P_3Sn_4$  phase from  $P_2Sn_5$  liquid using a machine learning (ML) interatomic potential with desirable efficiency and accuracy. Our results capture the liquid properties of  $P_2Sn_5$  at 1300 K, which is well above the melting temperature. The phase separation and crystallization are observed when  $P_2Sn_5$  liquid is cooled down below 832 and 505 K, respectively. The simulation results are in good agreement with the experimentally observed phase transformation behaviors and provide useful insights into the complex nucleation and crystallization process at the details of



atomistic scale. Our work also demonstrated that ML interatomic potentials based on neural network deep learning are robust and capable of accurately describing the energetics and kinetics of complex materials through molecular dynamics simulations.

### 1. INTRODUCTION

Metal phosphides have attracted considerable interest due to their promising physical and chemical properties for electronic applications. 1-3 However, metal phosphides, especially those with high phosphorus content (i.e., polyphosphides), are difficult to synthesize by direct combinations of the elements, because they need high temperatures and are companied by reactive byproducts.<sup>4</sup> At high temperatures, polyphosphides tend to decompose into lower phosphides and phosphorus vapor, whereas, at relatively low temperatures, the reactions are too slow to grow crystals in a reasonable time frame. This difficulty can be overcome using the low-melting-temperature metal (e.g., tin) flux growth method, and high-quality crystals of metal phosphides can be obtained. The low melting temperature (232 °C) makes tin an ideal metal flux, in which tin acting as a transporting medium dissolves the components in one place and grows the product at another location. Compared to the high-temperature direct synthesis method, the low-temperature tin-flux method avoids the thermodynamic traps and thus increases the odds for desirable compounds and/or phases. For example, the thermodynamically favored monoclinic NiP2 can be easily synthesized using the low-temperature tin-flux method. Moreover, the Re<sub>2</sub>P<sub>5</sub> compound was obtained only through the tin-flux method. In addition, liquid tin acts not only as solvents, but also as reactants, providing species which can be incorporated into a final product such as Cu<sub>4</sub>SnP<sub>10</sub>. Therefore, a fundamental understanding of the interactions among metal elements (M), P, and Sn and accurate computational modeling of the thermodynamics and growth kinetics of M-P-Sn systems, such as temperature dependence of phase stability and crystal nucleation and growth, are highly desirable in order to accelerate the discovery and synthesis of metal phosphide compounds for various modern technological applications.

Molecular dynamics (MD) simulation provides a useful computational tool to elucidate atomic details of the liquid, amorphous, and crystalline phases and provides atomistic insight into guiding the design and discovery of materials for various applications. However, an accurate and efficient description of the interatomic interactions plays a vital role in reliable MD simulations. While ab initio methods under the framework of density functional theory (DFT) are available to calculate the total energy and the forces on each atom based on the laws of quantum mechanics to ensure accurate MD simulations, such ab initio molecular dynamics (AIMD) is computationally very demanding and suffers from relatively smaller size (~500 atoms) and shorter simulation time (typically less than 1 ns). Alternatively, various empirical interatomic potential schemes, such as the Lennard-Jones potential, potentials based on the embedded atom method

Received: September 29, 2020 Revised: January 11, 2021 Published: January 28, 2021





(EAM),9 and the Stillinger-Weber potential,10 have been constructed for MD simulations. Based on physical considerations and reasonable approximations, these empirical interatomic potentials are usually analytic with some fitting parameters, which allows one to perform MD more efficiently than solving the quantum mechanics problem. However, the accuracy and transferability of these potentials is often in question. In addition, tuning the parameters of an empirical potential is usually a tedious task. Development of accurate empirical interatomic potentials for even pure P and Sn has been a challenging task due to several competing allotropic crystalline structures of P and Sn with different bonding characters. Most of the P and Sn interatomic potentials developed so far were constructed by the modified embedded atom method (MEAM). 11 The MEAM is an extension of the EAM formulation in which directional bonding is included in order to accurately describe the different local structures. The current MEAM models of P usually focus on a specific system, such as the P-Si system<sup>12</sup> and the P-Fe system. 13-16 The available MEAM models of Sn can describe various types of atomic bonds, including the metallic and covalent bonds; 17 however, these MEAM potentials were developed mostly focusing on properties of the liquid phase and showed deficiencies in reproducing physical properties of solid phases.<sup>22</sup> Furthermore, to the best of our knowledge, there are no P-Sn MEAM interatomic potentials.

In recent years, machine learning (ML) methods have emerged as a powerful tool to balance the accuracy and efficiency in the development of interatomic potentials. ML potentials usually do not require an explicit mathematical form as in the conventional empirical potentials and are trained on a set of reference data including potential energy and atomic forces of small systems, which can be obtained by accurate *ab initio* calculations. A number of promising ML approaches have been proposed. Some examples include the Behler–Parrinello neural network (BPNN), the Gaussian approximation potential (GAP), the gradient-domain machine learning method (GDML), the deep potential molecular dynamics scheme (DPMD), the deep potential molecular dynamics scheme (DPMD), the deep potential molecular dynamics scheme applied successfully to a variety of systems, from finite molecules to extended systems and from metallic systems to chemically bonded systems.

As a first step toward MD simulation studies of M-P-Sn ternary systems based on ML interatomic potentials, we develop an interatomic potential for the Sn-rich P-Sn system using the DPMD scheme (see the Supporting Information). P-Sn binaries can be considered as a special case of metal phosphides which contains complex interactions, i.e., covalent P-P interaction, metallic Sn-Sn interaction, and metalmetalloid P-Sn interaction. The special metal-metalloid bonding scheme makes P-Sn a system with unique properties, complemented by a wide range of compositions 32-38 and a complex phase diagram (see the Supporting Information). 39-41 Several binary tin phosphides, such as PSn and P<sub>3</sub>Sn<sub>4</sub>, have a layered structure. This special structure makes the P-Sn system exhibit a good electrochemical performance as anode materials and makes it a good catalyst for hydrogen evolution reactions. 42 P<sub>3</sub>Sn<sub>4</sub> and P<sub>3</sub>Sn are found to be anode materials for Na-ion batteries owing to their high volumetric specific capacity and good electrical conductivity. 43 P<sub>3</sub>Sn/C anodes can reversibly react with Na through conversion and alloy reaction processes, and this self-healing of alloy electrodes offers a new approach to explore novel superior electrode

materials for rechargeable batteries. In addition, nanostructured  $P_3Sn_4$  catalysts could photocatalytically degrade some typical organic dyes.<sup>44</sup>

In this paper, using MD simulations, we show that the neural network ML many-body interatomic potential for the P–Sn system developed by the DPMD scheme can accurately predict the temperature dependence of the phase stability of Sn-rich  $P_2Sn_5$  liquid and the crystallization of  $P_3Sn_4$  phases from  $P_2Sn_5$  liquid upon cooling.

#### 2. MD SIMULATION DETAILS

MD simulations are performed using a medium-size model (406 atoms) and large-size model (3248 atoms) with P<sub>2</sub>Sn<sub>5</sub> composition. The 406-atom model is used so that AIMD can be performed for the liquid state to validate the developed neural network potential (NNP). Periodic boundary conditions are applied in all three directions of the simulation box. The NVT ensemble (constant number of particles, constant volume, and constant temperature) with Nosé-Hoover thermostat is used in the simulations. A time step of 3 fs is used with the Verlet algorithm to integrate Newton's equations of motion. The AIMD simulation for liquid in the 406-atom model is performed using the Vienna Ab Initio Simulation Package (VASP). 45,46 The exchange and correlation energy is assessed by GGA in the scheme of Perdew-Burke-Ernzerhof (PBE).<sup>47</sup> Projector augmented wave (PAW)<sup>48</sup> pseudopotentials for P and Sn are used. A plane wave basis set with an energy cutoff of 255 eV and only the  $\Gamma$  point of the Brillouin zone are used. Classical MD simulations with the NNP are performed through the interface of the DEEPMD-KIT<sup>27</sup> to the LAMMPS code. 49 To compare the liquid structures obtained by AIMD and DPMD, the same simulation condition is applied, i.e., the same initial configurations, the same simulation steps, and the same NVT ensemble. However, since the atomic positions at each time step from AIMD and DPMD cannot be exactly the same, the comparison is meaningful only in the statistics sense (e.g., average energy, evolution trend of the energy, etc.).

# 3. RESULTS AND DISCUSSION

Figure 1 shows snapshots of the  $P_2Sn_5$  liquid at 1300 K from the AIMD and DPMD simulations. The snapshots of the 406-atom model from the AIMD and DPMD simulations are labeled as "AIMD<sub>406</sub>" and "DPMD<sub>406</sub>", respectively. It can be

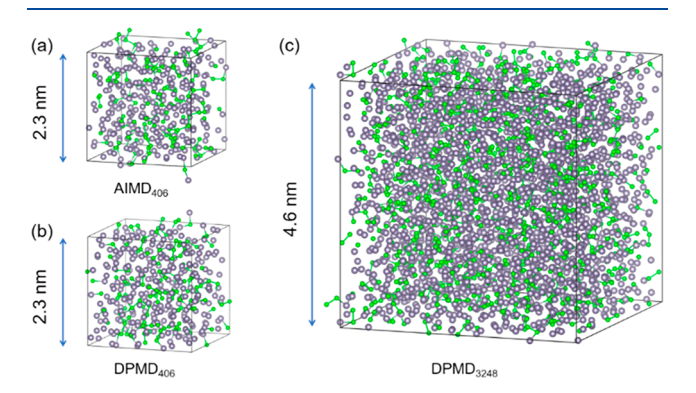


**Figure 1.** Snapshot structure of P<sub>2</sub>Sn<sub>5</sub> liquid at 1300 K from AIMD and DPMD simulations. (a) 406-atom model from AIMD, (b) 406-atom model from DPMD, and (c) 3248-atom model from DPMD. The large and small spheres represent Sn and P atoms, respectively.

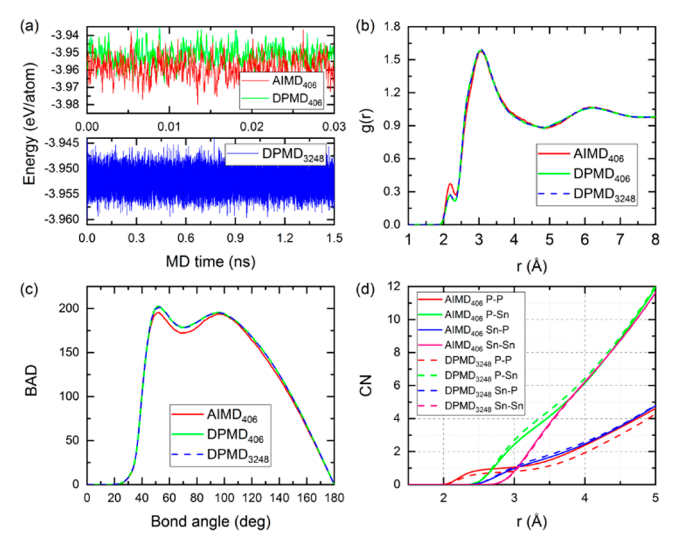


**Figure 2.** (a) Potential energy versus MD time, (b) total PCF, (c) total BAD, and (d) CN of liquid  $P_2Sn_5$  from the AIMD and DPMD at 1300 K.

seen that the distributions of the P atoms in the liquid from both the AIMD and DPMD simulations are similar. The potential energies of the AIMD<sub>406</sub> and DPMD<sub>406</sub> liquid as a function of time are shown in the upper panel of Figure 2a. The potential energies of AIMD<sub>406</sub> and DPMD<sub>406</sub> fluctuate with MD simulation time. The difference between the average energy from the AIMD and DPMD simulations is approximately 6.9 meV/atom, which is within the RMSE of the energy (9.5 meV/atom) in our NNP model when trained against ab initio calculation data. The MD simulation for largesize P<sub>2</sub>Sn<sub>5</sub> liquid at 1300 K using the NNP is performed for 1.5 ns (500,000 MD steps). This sample is labeled "DPMD<sub>3248</sub>", and the potential energy versus MD simulation time for this sample is illustrated in the lower panel of Figure 2a. The potential energy of DPMD<sub>3248</sub> fluctuates around a constant value with MD simulation time, indicating no phase transition or separation takes place at 1300 K, which is consistent with the P-Sn phase diagram.4

The local structures of the P<sub>2</sub>Sn<sub>5</sub> liquid at 1300 K are analyzed for the  $AIMD_{406}$ ,  $DPMD_{406}$ , and  $DPMD_{3248}$ . Total pair correlation functions (PCFs), total bond angle distributions (BADs), and coordination numbers (CN) are shown in Figure 2b-d. Very similar distributions are obtained for the liquid phase of P<sub>2</sub>Sn<sub>5</sub> at 1300 K between AIMD and DPMD. The total PCF peak positions of DPMD<sub>406</sub> coincide with that of AIMD<sub>406</sub>. The first PCF peak of liquid P<sub>2</sub>Sn<sub>5</sub> at 1300 K is located at 2.18 Å, corresponding to P-P interaction. The height of the first PCF peak of DPMD<sub>406</sub> is slightly lower than that of AIMD<sub>406</sub>, showing that NNP slightly underestimates the P-P interaction in the P<sub>2</sub>Sn<sub>5</sub> system. An excellent agreement of PCFs and BADs is observed for the DPMD<sub>406</sub> and DPMD<sub>3248</sub>, therefore confirming the validation of NNP for the large system. In addition, the comparison of the partial g(r)from AIMD and our DPMD is also shown in the Supporting Information. The underestimation of the nearest neighbor P-P correlation can be more clearly seen from the partial P-P g(r). While this discrepancy is the indication of the underestimation of the P-P nearest neighbor interaction in the NNP, some statistics error in the MD sampling would also contribute to the discrepancy, since the number of P atoms in the simulation cell is relatively much smaller.

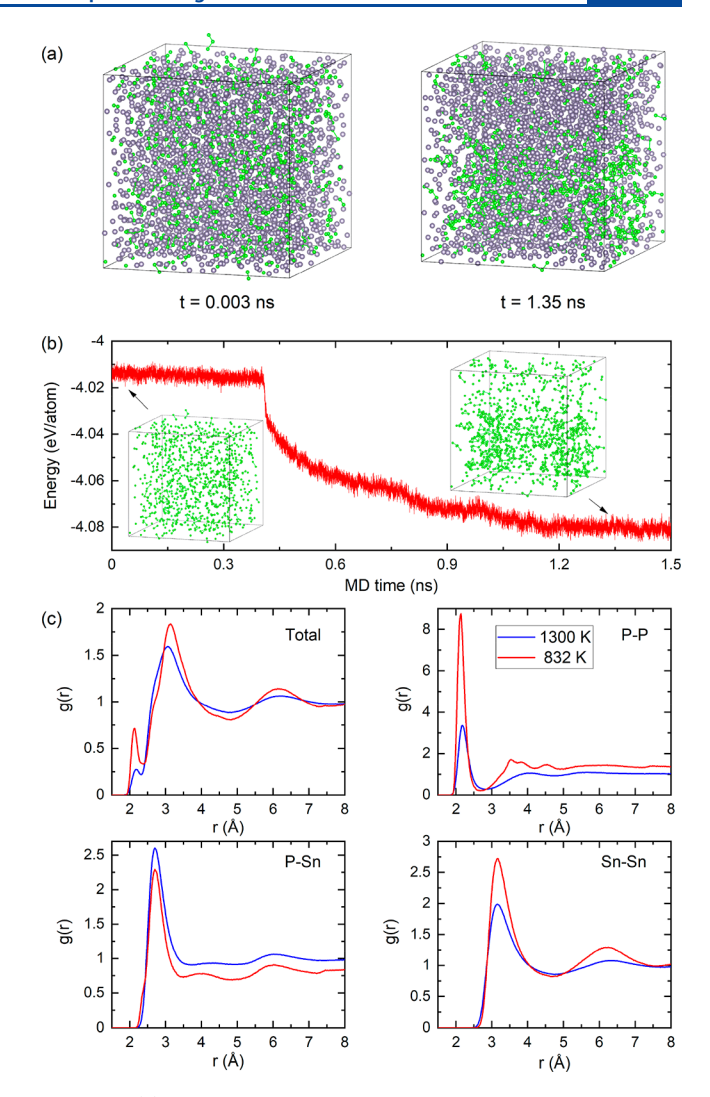


**Figure 3.** (a) Snapshots of all of the atoms in  $P_2Sn_5$  at 0.003 and 1.35 ns at 832 K. (b) Potential energy versus MD time of  $P_2Sn_5$  at 832 K with the snapshots at the MD simulation times of 0.003 and 1.35 ns, respectively, shown in the inset. Only P atoms (green sphere) are shown in these insets. (c) PCFs of  $P_2Sn_5$  at 1300 and 832 K.

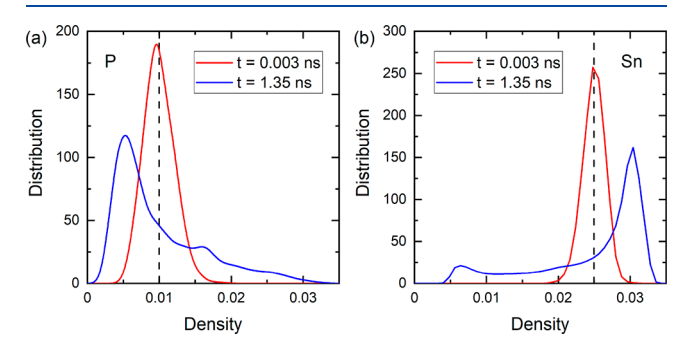


**Figure 4.** Histogram of the atomic density distribution of (a) P and (b) Sn in  $P_2Sn_5$  at 832 K at two different times. The vertical lines indicate the average atomic density.

The coordination number (CN) as a function of the cutoff distance r from the AIMD<sub>406</sub> and DPMD<sub>3248</sub> models is obtained by integrating the partial PCFs, as shown in Figure 2d. The coordination number of P–P for the AIMD<sub>406</sub> model is systematically larger than that for the DPMD<sub>3248</sub> model. If the bond length cutoffs are chosen to be 2.80 Å for the P–P

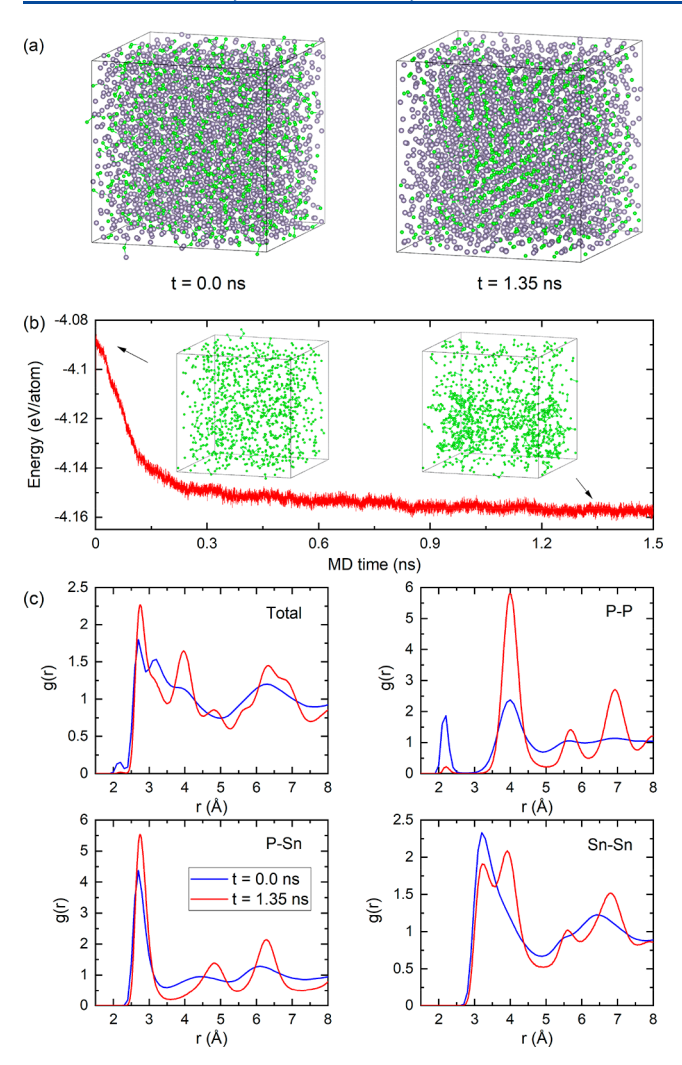


**Figure 5.** (a) Snapshots of all of the atoms in  $P_2Sn_5$  at 0.003 and1.35 ns at 505 K. (b) Potential energy versus MD time of  $P_2Sn_5$  at 505 K with the snapshots at the MD simulation times of 0.0 and 1.35 ns, respectively, shown in the inset. Only P atoms (green sphere) are shown in these insets. (c) PCFs of  $P_2Sn_5$  at the MD simulation times of 0.0 and 1.35 ns.

pair, 3.50 Å for the P-Sn pair, and 4.76 Å for the Sn-Sn pair, the P atom is coordinated by 1.0 P and 4.1 Sn atoms and the Sn atom is coordinated by 1.7 P and 10.1 Sn atoms in the AIMD<sub>406</sub> model. For the DPMD<sub>3248</sub> model, the P atom is coordinated by 0.7 P and 4.5 Sn atoms and the Sn atom is coordinated by 1.8 P and 10.2 Sn atoms. The discrepancy between AIMD and DPMD on the P-P coordination number would be an indication that the NNP underestimates the P-P interaction in the P2Sn5 system. In addition, we compare the diffusivity of P and Sn atoms between AIMD and DPMD simulations at 1300 and 800 K, as shown in Table S1. We find the DPMD slightly overestimates the diffusivity of both atoms. Because the crystallization rate is also dependent on the liquid diffusivity, 50 one would expect a slight overestimation of the crystallization speed from DPMD simulation for this system. Nevertheless, we do not expect any qualitative change on the phenomena reported here. More details about the calculation of the diffusion constant are given in section S2 of the Supporting Information.

After demonstrating the performance of NNP for the liquid, we turn our attention to the cooling process of P<sub>2</sub>Sn<sub>5</sub> to check

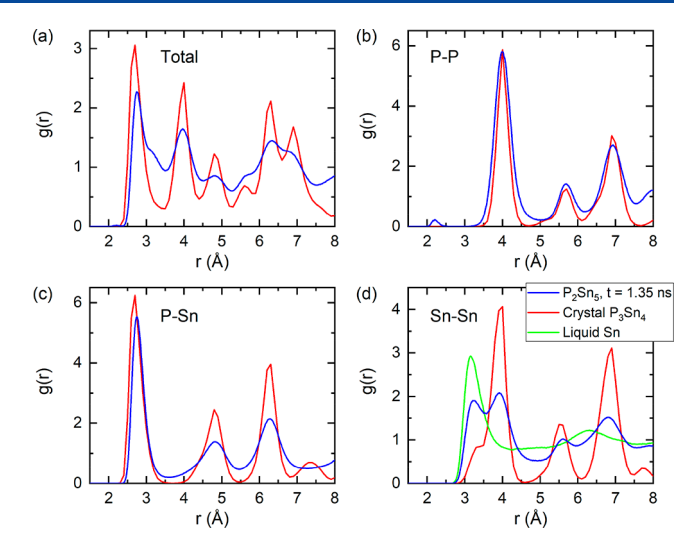


**Figure 6.** PCFs of  $P_2Sn_5$  at 1.35 ns, crystal  $P_3Sn_4$ , and liquid Sn at 505 K. (a) Total PCF, (b) P-P PCF, (c) P-Sn PCF, and (d) Sn-Sn PCF.

whether the NNP could capture the phase transformation behaviors. By carefully examining the P-Sn phase diagram, 41 we find that there are two characteristic temperatures, i.e., 832 and 505 K, for the system at the P<sub>2</sub>Sn<sub>5</sub> composition. Liquid P<sub>2</sub>Sn5 undergoes phase separation at 832 K and crystallization at 505 K. Therefore, we focus on MD simulations at 832 and 505 K, respectively, with the DPMD<sub>3248</sub> model to further verify the reliability of the NNP. The potential energy of P<sub>2</sub>Sn<sub>5</sub> vs MD time at 832 K using the DPMD<sub>3248</sub> model is displayed in Figure 3b. The potential energy of P<sub>2</sub>Sn<sub>5</sub> suddenly drops at around 0.4 ns and then smoothly decreases until 1.2 ns. The potential energy of P<sub>2</sub>Sn<sub>5</sub> drops approximately 16% during this process. Compared with the snapshot of P<sub>2</sub>Sn<sub>5</sub> at 0.003 ns, the P atoms segregate in the snapshot of 1.35 ns. These results indicate the phase separation of P<sub>2</sub>Sn<sub>5</sub>, which is consistent with the P-Sn phase diagram.<sup>41</sup>

Figure 3c shows the PCFs for  $P_2Sn_5$  at 832 K in comparison with those at 1300 K. It can be seen that the first peak in the total PCF and the first peak of the P–P partial PCF around 2.1 Å dramatically increase as the temperature drops from 1300 to 832 K. In addition, some new peaks emerge around 3.5 and 4.5 Å at 832 K, as shown in the P–P partial PCF. Meanwhile, the first and second peaks of the Sn–Sn partial PCF at 832 K become sharper than those at 1300 K. Accordingly, the PCF of P–Sn at 832 K decreases compared with that at 1300 K. These results clearly indicate that P and Sn atoms segregate from each other at 832 K, which is in agreement with the snapshot of  $P_2Sn_5$ , as shown in Figure 3b.

To further demonstrate the phase separation of  $P_2Sn_5$  at 832 K, we investigate the distribution of local atomic density at different MD simulation times. Here the local atomic density is computed by coarse graining the atomic distribution with a Gaussian smearing scheme as

$$D(\vec{r}) = \sum_{i} \left( \frac{1}{2\sigma^{2}\pi} \right)^{3/2} e^{-(\vec{r} - \vec{\eta}_{i})^{2}/2\sigma^{2}}$$

where  $\vec{r}_i$  is the position of atom *i*.  $\delta$  is the length of the first minimum in the PCF. The summation goes over all of the P or Sn atoms. In Figure 4a, the distribution of P density at 0.003 ns shows a single peak at the density of 0.01, indicating an overall

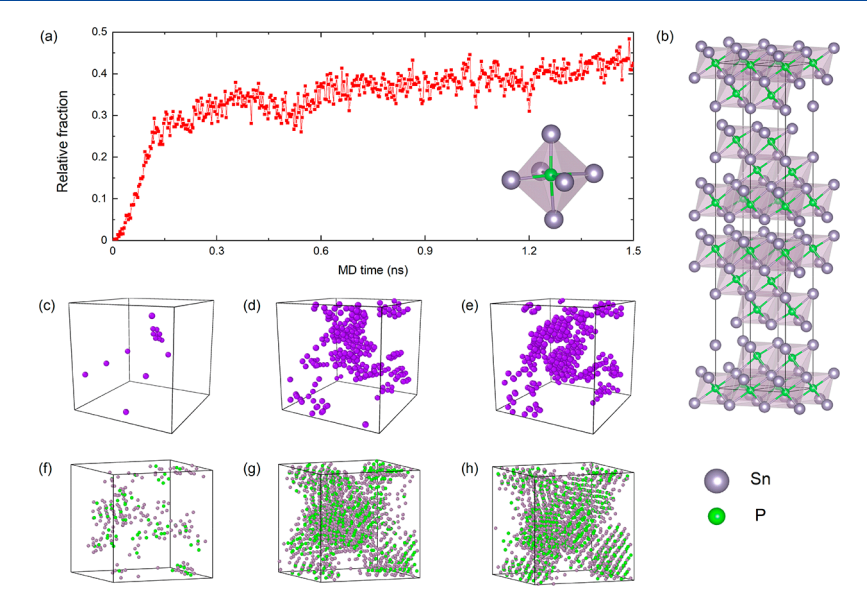


Figure 7. (a) The relative fraction of the P-centered octahedron of  $P_2Sn_5$  at 505 K in the MD simulation with the inset showing the P-centered octahedron. (b) Crystal structure of  $P_3Sn_4$ . (c-e) Snapshots in the MD simulation at 0.03, 0.3, and 1.35 ns. The purple sphere represents the P-centered octahedron. (f, g) Snapshots with the crystallized part in the MD simulation at 0.03, 0.3, and 1.35 ns.

uniform distributed state. This peak downshifts to 0.005 at 1.35 ns, and a small shoulder peak emerges at a higher density of 0.016. This indicates the P distribution becomes heterogeneous at the end of the MD simulations. Similarly, there is also one peak for the uniform distribution of Sn density at 0.003 ns, which is centered at 0.025, indicating that Sn is also homogeneously distributed at the beginning of the simulation at 832 K. At 1.35 ns, this peak moves upward to 0.030 and a small peak at the density of 0.006 appears, as shown in Figure 4b. Therefore, at 832 K, the system emerges a Sn-rich region at equilibrium. Based on the experimental phase diagram, <sup>41</sup> there exists a liquid—liquid separation at this region. The current heterogeneous density distribution indicates that the NNP well captures the phase separation in P<sub>2</sub>Sn<sub>5</sub> liquid below 832 K.

Next, we perform a MD annealing simulation for the DPMD<sub>3248</sub> model at 505 K. The potential energy decreases quickly in the first 0.3 ns and then smoothly decreases, as shown in Figure 5b. At the beginning of theMD simulation, P and Sn atoms are distributed homogeneously, as can be seen from the snapshot of the atomic structure at 0.0 ns in Figure 5a. A snapshot of the atomic distribution of P in the sample at 1.35 ns, as displayed in the inset of Figure 5b, shows that part of the P atoms tend to form ordered packing, indicating the crystallization of P<sub>2</sub>Sn<sub>5</sub> at 505 K, which is also seen in Figure 5a where all P and Sn atoms in the simulation box are plotted. The crystallization in the P<sub>2</sub>Sn<sub>5</sub> at 505 K can also be clearly seen by comparing the PCFs at the beginning (0.0 ns) and final stage (1.35 ns) of the simulation, as shown in Figure 5c. Compared to the total PCF of the P<sub>2</sub>Sn<sub>5</sub> snapshot at 0.0 ns, the total PCF peaks of the snapshot at 1.35 ns become sharper and narrower, indicating strong crystalline order. It should be noted that the first small peak located at 2.1 Å of the snapshot at 0.0 ns almost disappears in the snapshot at 1.35 ns. This small peak reflects the P-P interaction, which can be clearly seen from the top-right panel of Figure 5c. The first peak of the P-P partial PCF dramatically drops during the crystallization, whereas the second peak of the P-P partial PCF centered at 4 Å rises, indicating the breaking of the P-P chemical bonds.

The P atoms also tend to bond Sn atoms, which leads to the increase of the first peak of the P-Sn partial PCF, as shown in the bottom-left panel of Figure 5c.

According to the P–Sn phase diagram, <sup>41</sup> the P<sub>2</sub>Sn<sub>5</sub> phase could decompose into crystalline P<sub>3</sub>Sn<sub>4</sub> and liquid Sn phases. The changes in potential energy of P<sub>2</sub>Sn<sub>5</sub> at 505 K from our MD simulation imply the possible crystallization in the P–Sn system. To characterize the crystallized structure in the system, we calculate the total and partial PCFs of the crystalline P<sub>3</sub>Sn<sub>4</sub> and liquid Sn at 505 K and compare them with those of P<sub>2</sub>Sn<sub>5</sub> at 505 K and 1.35 ns, as shown in Figure 6. The peak positions of the PCF of the P<sub>2</sub>Sn<sub>5</sub> sample at 1.35 ns agree with those of the crystalline P<sub>3</sub>Sn<sub>4</sub> structure, as shown in Figure 6a–c. These results suggest the formation of the crystalline P<sub>3</sub>Sn<sub>4</sub> phase during the crystallization process. In addition, Figure 6d shows the first peak position of liquid Sn coincides with that of P<sub>2</sub>Sn<sub>5</sub> at 505 K, indicating that P<sub>2</sub>Sn<sub>5</sub> at 505 K is composed of the mixed liquid Sn and crystalline P<sub>2</sub>Sn<sub>5</sub> phases.

Crystal  $P_3Sn_4$  adopts a trigonal  $\overline{R}3m$  symmetry (space group no. 166). Each P atom is coordinated to six Sn atoms, forming a P-centered octahedron, as shown in the inset of Figure 7a. Thus, the representative structural element or fundamental building block is a P-center octahedron. To provide an intuitive picture of the crystallization process, the populations of P-center octahedra are computed with the cluster-alignment (CA) method.<sup>51</sup> Being a structural order parameter, the CA method can well differentiate complex crystal structures by computing the minimal root mean square deviation (RMSD) between the atomic cluster and the perfect crystal motifs. 52,50 With CA, the relative fraction of the P-center octahedron in the MD simulation box with respect to the simulation time is shown in Figure 7a. In the first 0.2 ns, the relative fraction of the P-centered octahedron dramatically increases, and then, it smoothly increases, which is similar to the trend of the potential energy change in Figure 5b. Approximately 33% P atoms form a P-centered octahedron at 0.2 ns, and it increases to 43% at 1.5 ns. Parts c-e of Figure 7 show the snapshots of the distribution of the P-centered octahedron at different MD simulation times. At 0.03 ns, there exists a small P-centered

octahedron as nuclei in the systems. With the increasing MD simulation time, multiple nuclei grow dramatically fast and form a few crystalline grains. The high nuclei density indicates a barrierless crystallization at current deep undercooling.

# 4. CONCLUSIONS

Using a many-body interatomic potential in neural-network representation through ML, DPMD simulations are performed to study the phase stability and transformation of P2Sn5 at different temperatures. The PCFs and BADs of liquid P2Sn5 obtained from the DPMD agree well with AIMD results, validating the accuracy of the ML interatomic potential for the complex P-Sn system. Upon cooling to 832 K, P<sub>2</sub>Sn<sub>5</sub> exhibits phase separation, which is verified by PCFs and atomic density distribution. Furthermore, the crystallization process is observed in the DPMD<sub>3248</sub> model of P<sub>2</sub>Sn<sub>5</sub> at 505 K. The precipitated crystal is identified to be crystalline P<sub>3</sub>Sn<sub>4</sub> by analyzing the PCFs of relevant liquid and crystal phases. The decrease of the first peak of the partial P-P PCF and increase of the first peak of the partial P-Sn PCF suggest that the P-P bonding breaks and the formation Sn-P bonds. The fundamental building block of P<sub>3</sub>Sn<sub>4</sub> is a P-centered octahedron, and its relative fraction increases with MD simulation time, which further provides more detailed insights into the crystallization process. The phase stability and transformation behavior of P2Sn5 obtained from our simulations are in excellent agreement with what would be expected from the known P-Sn binary phase diagram. Our results also suggest NNP by ML would be a promising avenue for MD simulation studies of phase stability and crystallization in complex M-P-Sn systems.

# ASSOCIATED CONTENT

#### Supporting Information

The Supporting Information is available free of charge at https://pubs.acs.org/doi/10.1021/acs.jpcc.0c08873.

Details of the neural network potential development and phase diagram of the P–Sn system (PDF)

#### AUTHOR INFORMATION

# **Corresponding Author**

Cai-Zhuang Wang — Ames Laboratory-USDOE and Department of Physics and Astronomy, Iowa State University, Ames, Iowa 50011, United States; oocid.org/0000-0002-0269-4785; Email: wangcz@ameslab.gov

#### **Authors**

Chao Zhang — Department of Physics, Yantai University, Yantai 264005, China; Ames Laboratory-USDOE, Iowa State University, Ames, Iowa 50011, United States;

orcid.org/0000-0002-5957-2287

Yang Sun — Department of Applied Physics and Applied Mathematics, Columbia University, New York 10027, United States; Orcid.org/0000-0002-4344-2920

Hai-Di Wang – Department of Physics and Astronomy, Iowa State University, Ames, Iowa 50011, United States

Feng Zhang – Ames Laboratory-USDOE, Iowa State University, Ames, Iowa 50011, United States

Tong-Qi Wen – Ames Laboratory-USDOE, Iowa State University, Ames, Iowa 50011, United States

Kai-Ming Ho – Department of Physics and Astronomy, Iowa State University, Ames, Iowa 50011, United States Complete contact information is available at: https://pubs.acs.org/10.1021/acs.jpcc.0c08873

#### **Author Contributions**

The manuscript was written through contributions of all authors. All authors have given approval to the final version of the manuscript.

#### Note

The authors declare no competing financial interest.

#### ACKNOWLEDGMENTS

C.Z. acknowledges the financial support from the National Natural Science Foundation of China (Grant No. 11874318) and the Natural Science Foundation of Shandong Province (Grant No. ZR2018MA043). Y.S. was supported by NSF Awards No. EAR-1918134 and No. EAR-1918126. Work at Ames Laboratory was supported by the U.S. Department of Energy (DOE), Office of Science, Basic Energy Sciences, Division of Materials Science and Engineering, including the computer time support on National Energy Research Scientific Computing Center (NERSC) in Berkeley, CA. Ames Laboratory is operated for the DOE by Iowa State University under Contract No. DE-AC02-07CH11358.

#### REFERENCES

- (1) Sharon, M.; Tamizhmani, G. Transition Metal Phosphide Semiconductors for Their Possible Use in Photoelectrochemical Cells and Solar Chargeable Battery (Saur Viddyut Kosh V). *J. Mater. Sci.* 1986, 21, 2193–2201.
- (2) Trindade, T.; O'Brien, P.; Pickett, N. L. Nanocrystalline Semiconductors: Synthesis, Properties, and Perspectives. *Chem. Mater.* **2001**, *13*, 3843–3858.
- (3) Hall, J. W.; Membreno, N.; Wu, J.; Celio, H.; Jones, R. A.; Stevenson, K. J. Low-Temperature Synthesis of Amorphous Fep<sub>2</sub> and Its Use as Anodes for Li Ion Batteries. *J. Am. Chem. Soc.* **2012**, *134*, 5532–5535.
- (4) Kanatzidis, M. G.; Pöttgen, R.; Jeitschko, W. The Metal Flux: A Preparative Tool for the Exploration of Intermetallic Compounds. *Angew. Chem., Int. Ed.* **2005**, *44*, 6996–7023.
- (5) Coleman, N.; Lovander, M. D.; Leddy, J.; Gillan, E. G. Phosphorus-Rich Metal Phosphides: Direct and Tin Flux-Assisted Synthesis and Evaluation as Hydrogen Evolution Electrocatalysts. *Inorg. Chem.* **2019**, *58*, 5013–5024.
- (6) Ruehl, R.; Jeitschko, W. Preparation and Crystal Structure of Dirhenium Pentaphosphide, Re<sub>2</sub>p<sub>5</sub>, a Diamagnetic Semiconducting Polyphosphide with Rhomboidal Re<sub>4</sub> Clusters. *Inorg. Chem.* **1982**, *21*, 1886–1891.
- (7) Honle, W.; von Schnering, H. G.  $Cu_4 \text{ snp}_{10}$ , a Compound with Decaphospha-Adamantane Anions  $P_{10}$  and Four-Center [Sncu<sub>3</sub>] Clusters. Z. Kristallogr. Cryst. Mater. **1980**, 153, 339–350.
- (8) Jones, J. E.; Chapman, S. On the Determination of Molecular Fields.—I. From the Variation of the Viscosity of a Gas with Temperature. *Proc. R. Soc. London, Ser. A* **1924**, *106*, 441–462.
- (9) Daw, M. S.; Baskes, M. I. Embedded-Atom Method: Derivation and Application to Impurities, Surfaces, and Other Defects in Metals. *Phys. Rev. B: Condens. Matter Mater. Phys.* **1984**, 29, 6443–6453.
- (10) Stillinger, F. H.; Weber, T. A. Computer Simulation of Local Order in Condensed Phases of Silicon. *Phys. Rev. B: Condens. Matter Mater. Phys.* **1985**, *31*, 5262–5271.
- (11) Baskes, M. I. Modified Embedded-Atom Potentials for Cubic Materials and Impurities. *Phys. Rev. B: Condens. Matter Mater. Phys.* **1992**, 46, 2727–2742.
- (12) Liu, B.; Zhang, H.; Tao, J.; Liu, Z.; Chen, X.; Zhang, Y. a. Development of a Second-Nearest-Neighbor Modified Embedded Atom Method Potential for Silicon-Phosphorus Binary System. *Comput. Mater. Sci.* **2016**, *120*, 1–12.

- (13) Ackland, G. J.; Mendelev, M. I.; Srolovitz, D. J.; Han, S.; Barashev, A. V. Development of an Interatomic Potential for Phosphorus Impurities In D-Iron. *J. Phys.: Condens. Matter* **2004**, *16*, S2629—S2642.
- (14) Barashev, A. V. Monte Carlo Simulation of Phosphorus Diffusion in (-Iron Via the Vacancy Mechanism. *Philos. Mag.* **2005**, 85, 1539–1555.
- (15) Ko, W.-S.; Kim, N. J.; Lee, B.-J. Atomistic Modeling of an Impurity Element and a Metal-Impurity System: Pure P and Fe-P System. *J. Phys.: Condens. Matter* **2012**, 24, 225002.
- (16) Ko, W.-S.; Park, J. Y.; Byun, J.-Y.; Lee, J.-K.; Kim, N. J.; Lee, B.-J. Manipulation of Surface Energy Anisotropy in Iron Using Surface Segregation of Phosphorus: An Atomistic Simulation. *Scr. Mater.* **2013**, *68*, 329–332.
- (17) Ravelo, R.; Baskes, M. Equilibrium and Thermodynamic Properties of Grey, White, and Liquid Tin. *Phys. Rev. Lett.* **1997**, *79*, 2482–2485.
- (18) Sapozhnikov, F. A.; Ionov, G. V.; Dremov, V. V.; Soulard, L.; Durand, O. The Embedded Atom Model and Large-Scale Md Simulation of Tin under Shock Loading. *J. Phys.: Conf. Ser.* **2014**, *500*, 032017.
- (19) Li, L. H.; Wang, W. L.; Wei, B. First-Principle and Molecular Dynamics Calculations for Physical Properties of Ni-Sn Alloy System. *Comput. Mater. Sci.* **2015**, *99*, 274–284.
- (20) Vella, J. R.; Chen, M.; Stillinger, F. H.; Carter, E. A.; Debenedetti, P. G.; Panagiotopoulos, A. Z. Structural and Dynamic Properties of Liquid Tin from a New Modified Embedded-Atom Method Force Field. *Phys. Rev. B: Condens. Matter Mater. Phys.* **2017**, 95, 064202.
- (21) Etesami, S. A.; Baskes, M. I.; Laradji, M.; Asadi, E. Thermodynamics of Solid Sn and Pbsn Liquid Mixtures Using Molecular Dynamics Simulations. *Acta Mater.* **2018**, *161*, 320–330.
- (22) Ko, W.-S.; Kim, D.-H.; Kwon, Y.-J.; Lee, M. H. Atomistic Simulations of Pure Tin Based on a New Modified Embedded-Atom Method Interatomic Potential. *Metals* **2018**, *8*, 900.
- (23) Behler, J. Perspective: Machine Learning Potentials for Atomistic Simulations. *J. Chem. Phys.* **2016**, *145*, 170901.
- (24) Behler, J.; Parrinello, M. Generalized Neural-Network Representation of High-Dimensional Potential-Energy Surfaces. *Phys. Rev. Lett.* **2007**, *98*, 146401.
- (25) Bartók, A. P.; Payne, M. C.; Kondor, R.; Csányi, G. Gaussian Approximation Potentials: The Accuracy of Quantum Mechanics, without the Electrons. *Phys. Rev. Lett.* **2010**, *104*, 136403.
- (26) Chmiela, S.; Tkatchenko, A.; Sauceda, H. E.; Poltavsky, I.; Schütt, K. T.; Müller, K.-R. Machine Learning of Accurate Energy-Conserving Molecular Force Fields. *Sci. Adv.* **2017**, *3*, No. e1603015.
- (27) Han, J.; Zhang, L.; Car, R.; E, W. Deep Potential: A General Representation of a Many-Body Potential Energy Surface. *Commun. Comput. Phys.* **2018**, 23, 629–639.
- (28) Wang, H.; Zhang, L.; Han, J.; E, W. Deepmd-Kit: A Deep Learning Package for Many-Body Potential Energy Representation and Molecular Dynamics. *Comput. Phys. Commun.* **2018**, 228, 178–184.
- (29) Zhang, L.; Han, J.; Wang, H.; Car, R.; E, W. Deep Potential Molecular Dynamics: A Scalable Model with the Accuracy of Quantum Mechanics. *Phys. Rev. Lett.* **2018**, *120*, 143001.
- (30) Wen, T.; Wang, C.-Z.; Kramer, M. J.; Sun, Y.; Ye, B.; Wang, H.; Liu, X.; Zhang, C.; Zhang, F.; Ho, K.-M.; Wang, N. Development of a Deep Machine Learning Interatomic Potential for Metalloid-Containing Pd-Si Compounds. *Phys. Rev. B: Condens. Matter Mater. Phys.* **2019**, *100*, 174101.
- (31) Bonati, L.; Parrinello, M. Silicon Liquid Structure and Crystal Nucleation from Ab Initio Deep Metadynamics. *Phys. Rev. Lett.* **2018**, *121*, 265701.
- (32) Olofsson, O.; Aava, U.; Haaland, A.; Resser, D.; Rasmussen, S. E.; Sunde, E.; Sørensen, N. A. X-Ray Investigations of the Tin-Phosphorus System. *Acta Chem. Scand.* **1970**, *24*, 1153–1162.
- (33) Gullman, J. The Crystal Structure of Snp. J. Solid State Chem. 1990, 87, 202-207.

- (34) Donohue, P. C. Synthesis, Structure, and Superconducting Properties of New High-Pressure Forms of Tin Phosphide. *Inorg. Chem.* **1970**, *9*, 335–337.
- (35) Katz, G.; Kohn, J. A.; Broder, J. D. Crystallographic Data for Tin Monophosphide. *Acta Crystallogr.* **1957**, *10*, 607.
- (36) Olofsson, O.; Jerslev, B.; Thom, E.; Stoll, E.; Eriksson, G.; Blinc, R.; Pausak, S.; Ehrenberg, L.; Dumanovic, J. On the Crystal Structure of Sn<sub>4</sub>p<sub>3</sub>. *Acta Chem. Scand.* **1967**, *21*, 1659–1660.
- (37) Ganesan, R.; Richter, K. W.; Schmetterer, C.; Effenberger, H.; Ipser, H. Synthesis of Single-Phase  $Sn_3p_4$  by an Isopiestic Method. *Chem. Mater.* **2009**, 21, 4108–4110.
- (38) Zaikina, J. V.; Kovnir, K. A.; Sobolev, A. N.; Presniakov, I. A.; Kytin, V. G.; Kulbachinskii, V. A.; Olenev, A. V.; Lebedev, O. I.; Tendeloo, G. V.; Dikarev, E. V.; Shevelkov, A. V. Highly Disordered Crystal Structure and Thermoelectric Properties of Sn<sub>3</sub>p<sub>4</sub>. *Chem. Mater.* **2008**, *20*, 2476–2483.
- (39) Zavrazhnov, A. Y.; Semenova, G. V.; Proskurina, E. Y.; Sushkova, T. P. Phase Diagram of the Sn-P System. *J. Therm. Anal. Calorim.* **2018**, *134*, 475–481.
- (40) Ritscher, A.; Schmetterer, C.; Ipser, H. Pressure Dependence of the Tin-Phosphorus Phase Diagram. *Monatsh. Chem.* **2012**, *143*, 1593–1602.
- (41) Okamoto, H. P-Sn (Phosphorus-Tin). J. Phase Equilib. 1993, 14, 263-264.
- (42) Liu, J.; Yu, G.; Zhang, R.; Huang, X.; Chen, W. Theoretical Predication of the High Hydrogen Evolution Catalytic Activity for the Cubic and Tetragonal Snp Systems. *Phys. Chem. Chem. Phys.* **2019**, 21, 5521–5530.
- (43) Kim, Y.; Kim, Y.; Choi, A.; Woo, S.; Mok, D.; Choi, N.-S.; Jung, Y. S.; Ryu, J. H.; Oh, S. M.; Lee, K. T. Tin Phosphide as a Promising Anode Material for Na-Ion Batteries. *Adv. Mater.* **2014**, *26*, 4139–4144.
- (44) Liu, S.; Li, S.; Li, M.; Yan, L.; Li, H. Synthesis of Tin Phosphides  $(Sn_4p_3)$  and Their High Photocatalytic Activities. *New J. Chem.* **2013**, 37, 827–833.
- (45) Kresse, G.; Furthmüler, J. Efficient Iterative Schemes for Ab Initio Total-Energy Calculations Using a Plane-Wave Basis Set. *Phys. Rev. B: Condens. Matter Mater. Phys.* **1996**, *54*, 11169–11186.
- (46) Kresse, G.; Joubert, D. From Ultrasoft Pseudopotentials to the Projector Augmented-Wave Method. *Phys. Rev. B: Condens. Matter Mater. Phys.* **1999**, *59*, 1758–1775.
- (47) Perdew, J. P.; Burke, K.; Ernzerhof, M. Generalized Gradient Approximation Made Simple. *Phys. Rev. Lett.* **1996**, *77*, 3865–3868.
- (48) Kresse, G.; Furthmüler, J. Efficiency of Ab-Initio Total Energy Calculations for Metals and Semiconductors Using a Plane-Wave Basis Set. *Comput. Mater. Sci.* **1996**, *6*, 15–50.
- (49) Plimpton, S. Fast Parallel Algorithms for Short-Range Molecular Dynamics. *J. Comput. Phys.* **1995**, *117*, 1–19.
- (50) Frenkel, Y. The Kinetic Theory of Liquids; Oxford University Press, 1946.
- (51) Fang, X. W.; Wang, C. Z.; Yao, Y. X.; Ding, Z. J.; Ho, K. M. Atomistic Cluster Alignment Method for Local Order Mining in Liquids and Glasses. *Phys. Rev. B: Condens. Matter Mater. Phys.* **2010**, 82, 184204.
- (52) Sun, Y.; Zhang, F.; Ye, Z.; Zhang, Y.; Fang, X.; Ding, Z.; Wang, C.-Z.; Mendelev, M. I.; Ott, R. T.; Kramer, M. J.; Ho, K.-M. 'Crystal Genes' in Metallic Liquids and Glasses. *Sci. Rep.* **2016**, *6*, 23734.
- (53) Sun, Y.; Ye, Z.; Zhang, F.; Jun Ding, Z.; Wang, C.-Z.; Kramer, M. J.; Ho, K.-M. Investigation of Partitionless Growth of E-Al<sub>60</sub> sm<sub>11</sub> Phase in Al-10 at% Sm Liquid. *Modell. Simul. Mater. Sci. Eng.* **2018**, 26, 015006.